Geospatial Perspective Reprojections for Ground-Based Sky Imaging Systems

Guillermo Terrén-Serrano and Manel Martínez-Ramón, *Senior Member, IEEE*

***Abstract*— The intermittency of solar energy produces instabilities in power grids. These instabilities are reduced with an intrahour solar forecast that uses ground-based sky imaging systems. Sky imaging systems use lenses to acquire images concentrating light beams in a sensor. The light beams received by the sky imager have an elevation angle with respect to the device's normal. Thus, the pixels in the image contain information from different areas of the sky within the imaging system field of view (FOV). The area of the FOV contained in the pixels increases as the elevation angle of the incident light beams decreases. When the sky imager is mounted on a solar tracker, the light beam's angle of incidence in a pixel varies over time. This investigation formulates and compares two geospatial reprojections that transform the original Euclidean frame of the imager's plane to the geospatial atmosphere cross section where the sky imager's FOV intersects the cloud layer. One assumes that an object (i.e., cloud) moving in the troposphere is sufficiently far so the Earth's surface is approximated *flat*. The other transformation takes into account the curvature of the Earth in the portion of the atmosphere (i.e., voxel) that is recorded. The results show that the differences between the dimensions calculated by both geospatial transformations are in the order of magnitude of kilometers when the Sun's elevation angle is below 30°.**

***Index Terms*— Perspective reprojection, sky imaging, solar forecasting, solar tracking.**

I. Introduction

THE global solar irradiance (GSI) that reaches the Earth's surface depends on shadows projected by moving clouds in the troposphere [1]. Consequently, clouds influence the energy generation in photovoltaic (PV) powered smart grids. GSI forecasting methods, which are efficient for intrahour horizons, analyze the dynamics of clouds to predict GSI minutes ahead of time using data acquired using ground-based sky imagers [2], to control the storage and dispatch of energy.

The horizons of intrahour solar forecasting depend on the field of view (FOV) of the sky imager used to acquire the images. A sky imager may be composed of one or multiple visible or infrared (IR) imagers, or both, and their FOV generally varies from 60° (low) to 180° (large). However, unless the sky imager is mounted on a solar tracker [3]–[5], the necessary FOV to perform an accurate intrahour solar forecast is large. Total sky imagers (TSIs) achieved large FOV sky images using a concave mirror to reflect light beams into a visible [6] or IR camera [7], and the camera is installed on a support at the focal distance of the mirror [8], [9]. An alternative to reflective sky imagers (in visible light sky images), is to increase the camera's FOV using a fisheye lens [10]–[13]. These are generally known as "all sky imagers" [14]–[16]. Similarly, the FOV of IR sky imagers can be enlarged applying image processing techniques to merge images acquired from multiple low FOV imagers [17].

Each of these sky imagers use light beams received at an angle with respect to the imager's plane. Therefore, the produced distortion should be corrected using a geometric transformation to compute the cloud velocity vectors. This method can be used to estimate the cloud-based size (i.e., area) but the cloud vertical dimension (i.e., thickness) is not available. The geometric transformation proposed by Nummikoski [18] transforms the Euclidean coordinate system of the pixels to a coordinate system based on the azimuth and elevation angles. This transformation was implemented by Richardson *et al.* [19] for reprojecting the pixels of a TSI, in the atmosphere cross section plane, using height measurements acquired using a nearby ceilometer. Ceilometers estimate the height of clouds and have been used to validate low-cost approaches to approximate the height of a cloud using multiple all sky imagers [20], [21]. However, this device is expensive and it is not applicable to more general operations such as a cloud speed sensor [22]. Another low-cost alternative to determine the velocity of clouds moving in the atmosphere cross section, and thus estimating their heights, was developed using an all sky imager and a grid of sensors (i.e., pyranometers) by Wang *et al.* [23].

Nevertheless, these geometric transformations were developed for static sky imagers (i.e., TSI and all sky imager). In contrast, the geospatial reprojections introduced in this investigation not only work for static sky imagers but are also applicable to sky imagers mounted on a solar tracker. In this last case, the perspective in the images is a function of the Sun's elevation and azimuth angles. The first approximation is a reprojection for devices that do not record low elevation angles (see Section II-B), while the second computes accurate reprojections even when the elevation angle is low (see Section II-C). The proposed reprojections were originally developed for a low FOV sky imager mounted on a solar tracker [24], [25], however, it is possible to obtain

Manuscript received November 11, 2021; revised January 26, 2022; accepted February 22, 2022. Date of publication February 24, 2022; date of current version April 5, 2022. This work was supported in part by the National Science Foundation (NSF) Established Program to Stimulate Competitive Research (EPSCoR) under Grant OIA-1757207 and in part by the King Felipe VI Endowed Chair of The University of New Mexico (UNM). *(Corresponding author: Guillermo Terrén-Serrano.)*

The authors are with the Department of Electrical and Computer Engineering, The University of New Mexico, Albuquerque, NM 87131 USA (e-mail: guillermoterren@unm.com; manel@unm.edu).

Digital Object Identifier 10.1109/TGRS.2022.3154710

the geospatial reprojection for any FOV and elevation angle by reparameterizing the algorithms. As a ceilometer was not available, the proposed methods applies the moist adiabatic lapse rate (MALR) to avoid the need for ceilometer measurements. The estimation of the error in the height approximation using this method is out of the scope of this investigation.

II. Methodology

A. Rectilinear Lens

The acquired image is the light beam refraction in a converging point of the emitted blackbody radiation. The image resolution is defined as $N \times M$ pixels. If the radiant objects (the Sun and the clouds) are at a distance $z \to \infty$, the radiation rays converge at the focal length. Consequently,

$$\frac{1}{f} = \frac{1}{z} + \frac{1}{D} \approx \frac{1}{D} \tag{1}$$

where f is the focal length and D is the distance from the lens to the converging point. The relation between the diagonal FOV and the focal length f for a rectilinear lens is

$$\tan \frac{\text{FOV}}{2} = \delta \frac{N_{\text{diag}}}{2f} \tag{2}$$

where $N_{\text{diag}} = (N^2 + M^2)^{1/2}$ is the number of pixels in the diagonal of the sensor and δ is the pixel size. Therefore, the focal length f of camera is

$$f = \frac{\delta}{2} \frac{N_{\text{diag}}}{\tan \frac{\text{FOV}}{2}}. \tag{3}$$

B. Flat Earth Approximation

The *flat* Earth approximation is viable without large error (when the elevation of the Sun ε_0 is higher than 30°) because the portion of the Earth's atmosphere in the FOV of the camera is much smaller than its entire surface. With this assumption, the reprojection from the imager plane to the atmosphere cross-section plane (in Fig. 1) is obtained with the distance z of a cloud to the camera lens. The distance z is a function of the cloud height h and the elevation angle ε of the cloud in a pixel

$$z = \frac{h}{\sin \varepsilon}. \tag{4}$$

The cloud height was estimated using the elevation angle ε of the cloud in a pixel and the MALR model [26]

$$\begin{aligned} \Gamma_{\text{MALR}} &= g \frac{1 + \frac{L_r \cdot r_r}{R \cdot T^{\text{air}}}}{c_{\text{pd}} + \frac{L_p^2 r_p \varepsilon}{R\left(T^{\text{air}}\right)^2}} \\ &= g \frac{R_{\text{sd}}\left(T^{\text{air}}\right)^2 + H_v r_v T^{\text{air}}}{c_{\text{pd}} R_{\text{sd}}\left(T^{\text{air}}\right)^2 + H_v^2 r_v \epsilon} \text{ [K/m]}. \end{aligned} \tag{5}$$

Here, the following holds.

1) Earth's gravitational acceleration, $g = 9.8076$ m/s^2.
2) Water vaporization heat $H_v = 2501000$ J/kg.
3) Dry air specific gas constant $R_{\text{sd}} = 287$ J/kg K.
4) Water vapor specific gas constant $R_{\text{sw}} = 461.5$ J/kg K.

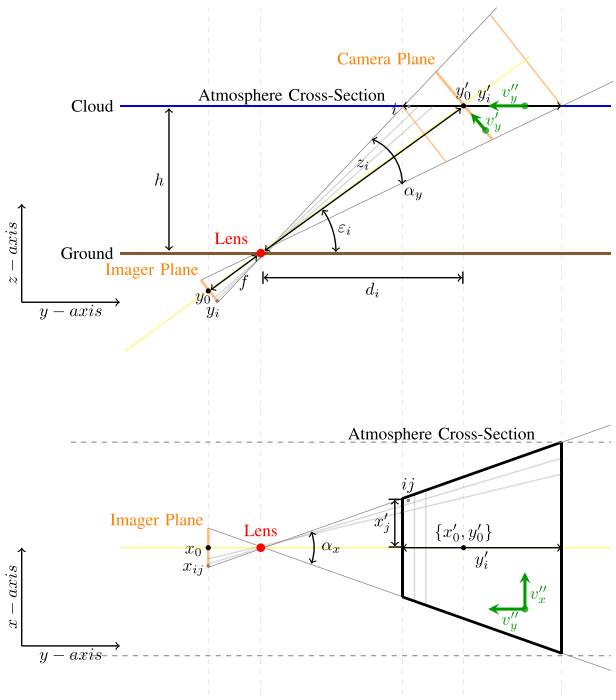

Fig. 1. *Flat* Earth geospatial reprojection. (Top) Geospatial reprojection y-axis or side view, which shows how the reprojection depends on the distance z_i of an object to the imager, the height h and the elevation ε_i. (Bottom) Geospatial reprojection x-axis or top view, which shows the relation of the angular increments α used to compute the elevation angle ε_i of each one of the pixels ij in the image. The velocity decomposition $\mathbf{v}' = \{v'_x, v'_y\}$ shows that cloud velocity components have a perspective distortion in the x-axis and in the y-axis, due to the camera plane inclination of ε degrees with respect to the normal. x'_j and y'_i represent the coordinates of the pixel in the image [see (9)]. When the coordinate system is centered applying (23), $\mathbf{x}_0 = \{x'_0, y'_0\}$ represent the origin of coordinates.

5) Dimensionless ratio of dry air specific gas constant to water vapor specific gas constant $\epsilon = R_{\text{sd}}/R_{\text{sw}} = 0.622$.
6) Saturated air water vapor pressure, $e = \epsilon \cdot \exp([7.5T^{\text{dew}}]/[273.3 + T^{\text{dew}}]) \cdot 100$. The original formula is in hPa but this is onen in Pa.
7) Mixing ratio of water vapor mass to dry air mass $r_v = [\epsilon \cdot e]/[p^{\text{atm}} - e]$.
8) Dry air specific heat at constant pressure $c_{\text{pd}} = 1003.5$ J/kg K.

The ratio Γ_{MALR} is fully described knowing the air temperature T^{air}, the atmospheric pressure p^{atm} and the dew point T^{dew}. Γ_{MALR} is used to calculate the cloud height in the radiometric IR image defined as $\mathbf{T} = \{T_{i,j} \in \mathbb{B} \mid \forall i = 1, \ldots, M, \ \forall j = 1, \ldots, N\}$ in Kelvin

$$H_{i,j} = \frac{\left(T_{i,j} - T^{\text{air}}\right)}{\Gamma_{\text{MALR}}} \ [m]. \tag{6}$$

A cloud in the sky images are segmented indicating which the pixels belong to a cloud, so that $\mathbf{B} = \{b_{i,j} \in \mathbb{B} \mid \forall i = 1, \ldots, M, \ \forall j = 1, \ldots, N\}$ is a binary image where 0 is a clear sky pixel, and 1 is cloudy pixel [5]. The cloud height in a frame are computed using only in the cloudy pixels

$$h = \frac{\sum_{i,j} H_{i,j} \cdot \mathbb{I}\left(b_{i,j} = 1\right)}{\sum_{i,j} H_{i,j} \cdot \mathbb{I}\left(b_{i,j} = 1\right)} \tag{7}$$

where $\mathbb{I}(\cdot)$ is the indicator function.

The reprojection is computed with respect to the coordinates of each pixel ij in the imager plane. The coordinates of a pixel in the imager plane are defined as $x_j = j\delta$ and $y_i = i\delta$. In this reprojection, we assume that the elevation angle ε_i is different in each row i and constant in each column j of pixels in an image, and the differential angle α_j (formed by the position of Sun and a pixel) is different in each column j and constant in each row i of pixels. This assumption is valid since the FOV of the individual pixels in the rectilinear lens is sufficiently small. As seen in Fig. 1, when intersecting a cloud layer, the projection of the 3-D pyramid defined by the camera FOV in a 2-D plane forms a trapezoid. The elevation ε_i and azimuth α_j angles for each pixel ij are

$$\boldsymbol{\varepsilon} = \left\{ \left(\varepsilon_0 + i\frac{\nu}{2}\right) \;\middle|\; \varepsilon_i \in \mathbb{R}^{(0,\pi]},\ \forall i = -\frac{N}{2}, \ldots, \frac{N}{2} \right\}$$
$$\boldsymbol{\alpha} = \left\{ \left(\alpha_0 + j\frac{\nu}{2}\right) \;\middle|\; \alpha_j \in \mathbb{R}^{(0,\alpha_x/2]},\ \forall j = -\frac{M}{2}, \ldots, \frac{M}{2} \right\} \tag{8}$$

where $\nu = [\text{FOV}/(N^2 + M^2)^{1/2}] \cdot [\pi/180]$ is the camera ratio in radians per pixel, ε_0 is the Sun's elevation angle, and $\alpha_0 = 0$. Therefore, $\alpha_j = 0$ and $\varepsilon_i = \varepsilon_0$ represent the center of the image (since $\alpha_0 = 0$), but only when the number of pixels N and M are odd numbers. For all pixels, ν is approximated by a constant. In this way, the FOV is $\alpha_x = \nu M$ and $\alpha_y = \nu N$ in the x- and y-axes, respectively.

The length of a row of pixels j reprojected in the atmosphere cross section is $x'_{ij} = x_j \cdot z_i / f$, so substituting z_i in (4), the coordinates of the imager plane reprojected in the atmosphere cross section are

$$x'_{ij} = \frac{x_j}{f} \cdot z_i = \frac{x_j}{f} \cdot \frac{h}{\sin\varepsilon_i}$$
$$y'_i = \frac{y_i}{f} \cdot z_i = \frac{y_i}{f} \cdot \frac{h}{\sin\varepsilon_i}. \tag{9}$$

C. Great Circle Approach

The atmosphere cross-section plane can be approximated more exactly using the pyramid formed by the camera FOV when intersects a cloud layer at height h in point D in Fig. 2. The assumption is that the Earth and the cloud layer surface are two perfect spheres. The *great* circle is defined as the cloud layer surface at height h, and *small* circle is the Earth's surface. The tangent plane to the Earth's surface which intersects with the cloud layer is the chord AB (see Fig. 2). The Earth's radius is r_{Earth}. The sagitta $\ell_i = h - v_i$ is the length from the middle of chord C_iD_i to the cloud layer, and v_i is the perpendicular distance from the *great* circle to the *small* circle. The *great* and *small* circles radii are, respectively,

$$R = r + h$$
$$r = r_{\text{Earth}} + \rho \tag{10}$$

where ρ is the altitude above the sea level of the localization where the sky imager is installed.

The imager elevation angle ε_i defines the triangle formed by the line z_i that intersect the Earth's surface and the cloud layer as

$$\tan\varepsilon_i = \frac{v_i}{w_i}. \tag{11}$$

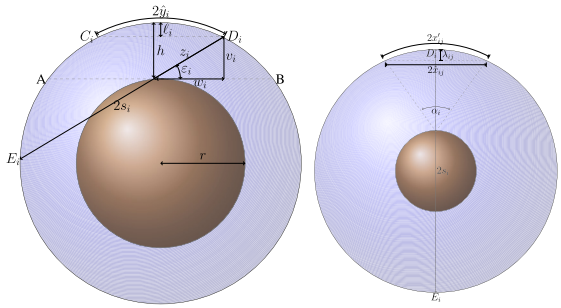

Fig. 2. Drawing of the *great* circle (surface of a cloud layer) and the *small* circle (Earth's surface). The key in this approach is to find the relation between the chords C_iD_i and AB to calculate y'_i (see right drawing, which is the imager's y-axis view). Similarly, x'_{ij} is computed for each y'_i, using the circle with diameter $2s_i$, formed by chord D_iE_i (see left drawing, which is the imager's x-axis view).

By taking this approach, the geospatial reprojection coordinates are calculated with respect to the imager lens.

1) Reprojection of the y-Axis: The sagitta ℓ_i of chord C_iD_i is related to the chord AB (see Fig. 2). The formula that describes the sagitta ℓ_i is a function of the triangle formed by the intersecting line z_i that goes from AB to C_iD_i with elevation angle ε_i

$$\begin{aligned}
\ell_i &= R - \sqrt{R^2 - w_i^2} \\
h - v_i &= R - \sqrt{R^2 - w_i^2} \\
R^2 - w_i^2 &= (w_i \tan\varepsilon_i + r)^2 \\
R^2 - w_i^2 &= w_i^2 \tan^2\varepsilon_i + r^2 + 2r w_i \tan\varepsilon_i \\
(r+h)^2 &= w_i^2 \tan^2\varepsilon_i + 2r w_i \tan\varepsilon_i + w_i^2 + r^2 \\
h^2 + 2rh &= w_i^2\left(1 + \tan^2\varepsilon_i\right) + 2r w_i \tan\varepsilon_i \\
0 &= w_i^2\left(1 + \tan^2\varepsilon_i\right) + w_i(2r\tan\varepsilon_i) - h(h+2r)
\end{aligned} \tag{12}$$

where $\ell_i = h - v_i$, $v_i = w_i \tan\varepsilon_i$ and $R = r + h$. The quadratic equation has following coefficients:

$$\begin{aligned}
a_i &= 1 + \tan^2\varepsilon_i \\
b_i &= 2r\tan\varepsilon_i \\
c_i &= -h(h+2r).
\end{aligned} \tag{13}$$

The length of triangle side w_i is the result obtained solving the quadratic formula

$$w_i = \frac{-b_i + \sqrt{b_i^2 - 4a_ic_i}}{2a_i}, \quad w_i \in \mathbb{R}^+. \tag{14}$$

When $r \to \infty$, $w_i \approx d$ and $v_i \approx h$, thus the *flat* approximation is equivalent to the *great* circle approach $w_i \approx h/\tan\varepsilon_i$.

The *great* circle segment $\hat{y}_i$ is the distance from the center of the arc defined by the saggita ℓ_i to the point D_i (see Fig. 2). The chord $2w_i$ is projected to the arc $2\hat{y}_i$ of the *great* circle by applying the arc formula

$$\hat{y}_i = R \arcsin\frac{w_i}{R}. \tag{15}$$

Each pixel in an image has a different elevation angle ε_i that corresponds to a point D_i in the *great* circle. Therefore,

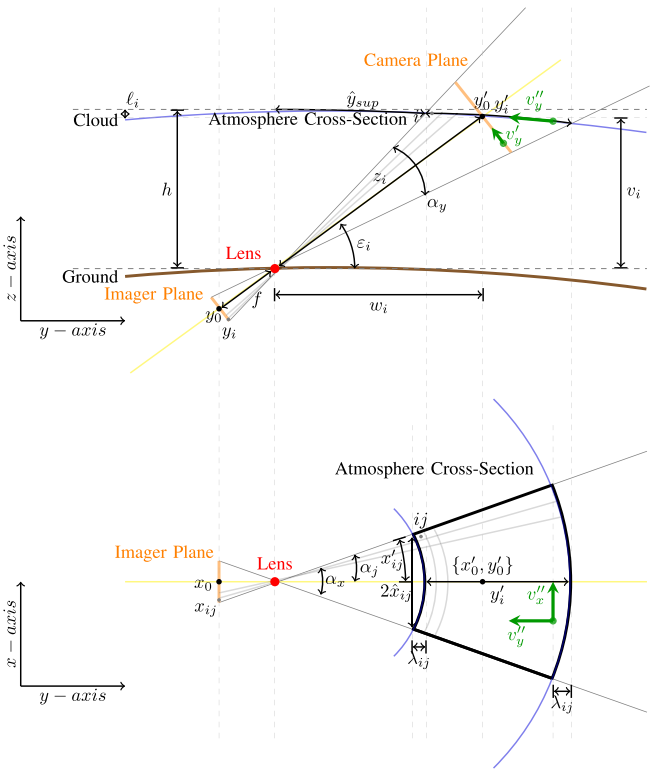

Fig. 3. (Top) *Great* circle geospatial reprojection in the y-axis or side view. (Bottom) x-axis or top view. *Imager Plane* and *Lens* are parts of the sky imager. They are physically separated by a focal length f. The distance z_i from the lens to the cloud layer is detailed in the top graph. x'_j and y'_i represent the coordinates of the pixel in the image [see (16) and (22)].

the coordinates of the pixels relative to the imager lens in the atmosphere cross-section plane are calculated by subtracting them the distance $\hat{y}_{\text{sup}}$ which has the highest elevation [see Fig. 3 (top)]

$$y'_i = \hat{y}_i - \hat{y}_{\text{sup}} \quad \forall i = 1, \ldots, N. \tag{16}$$

2) Reprojection of the x-Axis: The reprojection of the imager plane x-axis to the atmosphere cross section is a function of the distance $z_i^2 = w_i^2 + v_i^2$ from the imager plane to the cloud layer, and the chord $2\hat{x}_{ij}$ of segment the $2x'_{ij}$ formed by the angle α_j [see Fig. 3 (bottom)]

$$\hat{x}_{ij} = \left(z_i - \lambda_{ij}\right) \tan \alpha_j \quad \forall i = 1, \ldots, M, \;\; j = 1, \ldots, M. \tag{17}$$

The diameter of the small circle $2s_i$, which is the chord $D_i E_i$ in Fig. 2, is obtained by applying the intersecting chord theorem. In Euclid's Elements Book III [27, Proposition 35], the intersecting chords theorem is defined as $|\text{AS}| \cdot |\text{SC}| = |\text{BS}| \cdot |\text{SD}| = r^2 - d^2$. When this theorem is applied to our problem the corresponding variables are $d = (R - h)$, $r = R$, $|\text{AS}| = s_i - z_i$ and $|\text{SC}| = z_i$ (see Fig. 2 y-axis graph), so

$$\begin{aligned} (2s_i - z_i) z_i &= R^2 - (R - h)^2 \\ s_i &= \frac{2Rh - h^2}{2z_i} + \frac{z_i}{2}. \end{aligned} \tag{18}$$

The relation between the arc length $2x'_{ij}$ and the chord $2\hat{x}_{ij}$ is found through the sagitta λ_{ij}. The formula which describes

$$\begin{aligned} 0 &= \hat{x}_{ij}^2 - \left(2s_i - \lambda_{ij}\right)\lambda_{ij} \\ 0 &= \lambda_{ij} + \frac{\hat{x}_{ij}^2}{\lambda_{ij}} - 2s_i \\ 0 &= \left(z_i - \lambda_{ij}\right)^2 \tan^2 \alpha_j + \lambda_{ij}^2 + 2s_i \lambda_{ij} \\ 0 &= \lambda_{ij}^2 \left(1 + \tan^2 \alpha_j\right) - 2\lambda_{ij}\left(z_i \tan^2 \alpha_j - s_i\right) + z_i^2 \tan^2 \alpha_j \end{aligned} \tag{19}$$

where coefficients for solving the quadratic formula are

$$\begin{aligned} a_{ij} &= 1 + \tan^2 \alpha_j \\ b_{ij} &= -2s_i - 2z_i \tan^2 \alpha_j \\ c_{ij} &= z_i^2 \tan^2 \alpha_j. \end{aligned} \tag{20}$$

The sagitta λ_{ij} is the result obtained solving (19)

$$\lambda_{ij} = \frac{-b_{ij} - \sqrt{b_{ij}^2 - 4a_{ij}c_{ij}}}{2a_{ij}}, \quad \lambda_{ij} \in \mathbb{R}^+. \tag{21}$$

When $r \to \infty$, $s_i \to \infty$, in consequence $\lambda_{ij} \approx 0$ and $x'_{ij} \approx \hat{x}_{ij}$. The *flat* Earth approximation is equivalent to the *great* circle approach.

The arc length $2x'_{ij}$ is calculated knowing the sagitta λ_{ij} and the small radius s_i

$$x'_{i,j} = s_i \arcsin\left[\frac{\left(z_i - \lambda_{ij}\right)\tan \alpha_j}{s_i}\right] \tag{22}$$

where segment $x'_{i,j}$ is the projection of x-axis in the atmosphere cross-section plane.

The origin of the coordinate system can be defined at the position of the Sun

$$\begin{aligned} x''_{ij} &= x'_{ij} - x'_0 \\ y''_{ij} &= y'_{ij} - y'_0 \end{aligned} \tag{23}$$

where $\mathbf{x}'_0 = \{y'_0, x'_0\}$ are the pixel index of the Sun position in the image. These equation is applicable to both proposed perspective reprojections.

III. Results and Discussion

The geospatial perspective reprojections are applied to a sky imager mounted on a solar tracker that updates its pan and tilt every second, maintaining the Sun in a central position in the images throughout the day. The sky imager is located in the Electrical and Computer Engineering (ECE) Department at the University of New Mexico (UNM) central campus in Albuquerque. The climate of Albuquerque is arid semicontinental, with minimal rain, which is more likely in the summer months. The ECE Department is approximately located 1250 m away (i.e., linear distance) from the city center whose elevation is 1620 m with respect to sea level.

The IR sensor is a Lepton[1] 2.5 radiometric camera with wavelength from 8 to 14 μm. Pixel intensity within the frame is measured in centikelvin units. The resolution of an IR

[1]https://www.flir.com/

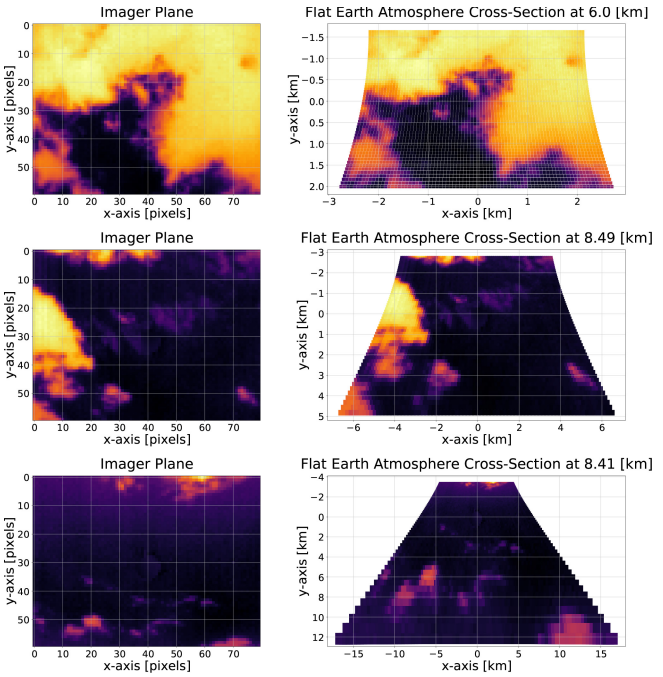

Fig. 4. (Left) Three sky images taken at different elevation angles: 71.06°, 50.17°, and 30.83° (from top to bottom). (Right) Column shows the same three images after applying the geospatial perspective reprojection using the *flat* Earth approximation.

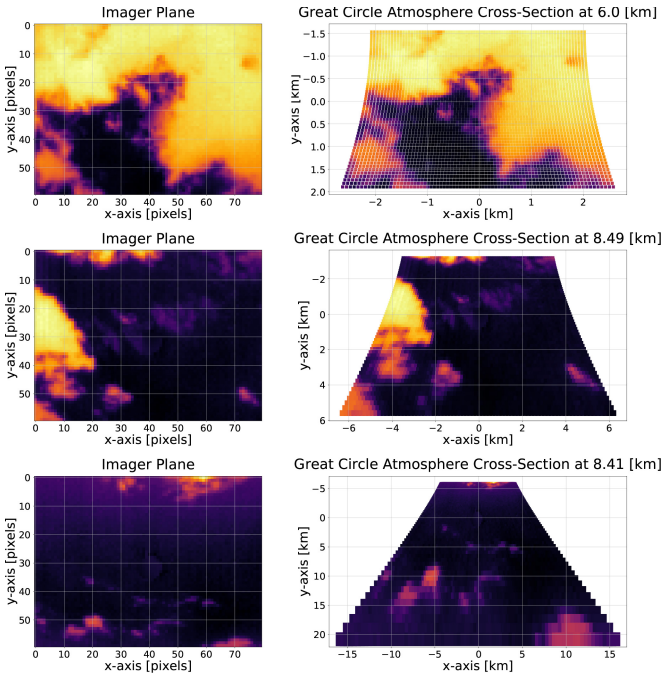

Fig. 5. (Left) Three sky images taken at different elevation angles: 71.06°, 50.17°, and 30.83° (from top to bottom). (Right) Resulting sky images after applying the geospatial perspective reprojection using the *great* circle approach.

image is 80 × 60 pixels. To implement the reprojection, the manufacturing specifications of the camera used are: 63.75° diagonal FOV, 51° horizontal FOV_x, 38.25° vertical FOV_y, and the size of a pixel is $\delta = 17\ \mu$m. When other lenses (e.g., fisheye) are used, the camera lens affine reprojection must first be computed to know the FOV of each pixel.

The pixels in Figs. 4 and 5 are displayed in the camera pixel coordinates (left) and in the atmosphere cross-section plane (right). The pixels are scaled to their actual size in the atmosphere cross-section plane. The distortion produced by the sky imager perspective causes the atmosphere cross-section plane dimensions to increase when the elevation angle decreases (see Fig. 6).

The difference between both geospatial reprojections is measured using root mean square error (RMSE). The coordinates computed using the *flat* Earth assumption are $\mathbf{X}_1, \mathbf{Y}_1$, and the coordinates computed using *great* circle approach are $\mathbf{X}_2, \mathbf{Y}_2$. The RMSE, defined as $E(\cdot)$, is calculated for each pixel averaging together the difference residuals computed independently in coordinates x and y

$$E(\mathbf{X}_1, \mathbf{X}_2, \mathbf{Y}_1, \mathbf{Y}_2) = \sqrt{\frac{1}{2}[\mathcal{R}(\mathbf{X}_1, \mathbf{X}_2) + \mathcal{R}(\mathbf{Y}_1, \mathbf{Y}_2)]}. \quad (24)$$

The residuals are $\mathcal{R}(\mathbf{X}_1, \mathbf{X}_2) = (\mathbf{X}_1' - \mathbf{X}_2')^2$ for each coordinate.

The error maps (see Fig. 7) show the differences between the coordinate systems approximated by both reprojections. The symmetry between both reprojections is not perfectly circular. This is because the elevation angle in *flat* Earth reprojection, was approximated as constant across the pixels in the same row.

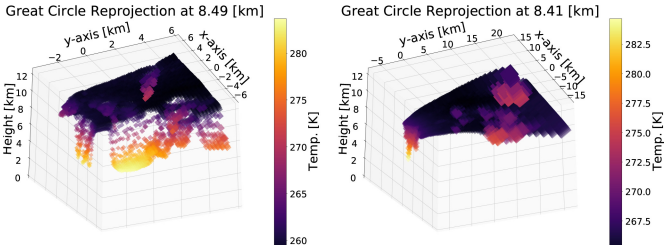

Fig. 6. Graphs show the resulting sky images after applying the *great* circle geospatial perspective reprojection. (Left) Sky image taken at an elevation angle of 50.17°. (Right) Sky image taken at an elevation angle of 30.83°.

The tropopause average height is approximately 10 km in the latitude where the sky imager is located depending on the season. The first image in Fig. 7 shows the error map when the camera is at the zenith. The magnitude order of the error is in meters when $\varepsilon \geq 30°$. However, when the Sun's elevation angle is below $\varepsilon < 30°$ the magnitude order of the error is in kilometers. Taking this into account, the geospatial reprojection that assumes that the Earth's surface is *flat*, is only adequate when the elevation angle of a sky imager pixel is above $\varepsilon \geq 30°$. If the sky imager is designed to operate below $\varepsilon < 30°$, the most suitable reprojection is computed using the great circle approach.

The difference between both transformations in the magnitude of the error is due to the dimensions of the region of the atmosphere that is being measured with the sky imager (see Fig. 8). For an image at height h and elevation ε, we compute the total RMSE $\boldsymbol{E}(h, \varepsilon)$ as the square root of sum of errors $E(\mathbf{X}_1, \mathbf{X}2, \mathbf{Y}_1, \mathbf{Y}_2)$ for all coordinates of the image. Fig. 8 (left) shows a representation of this error for

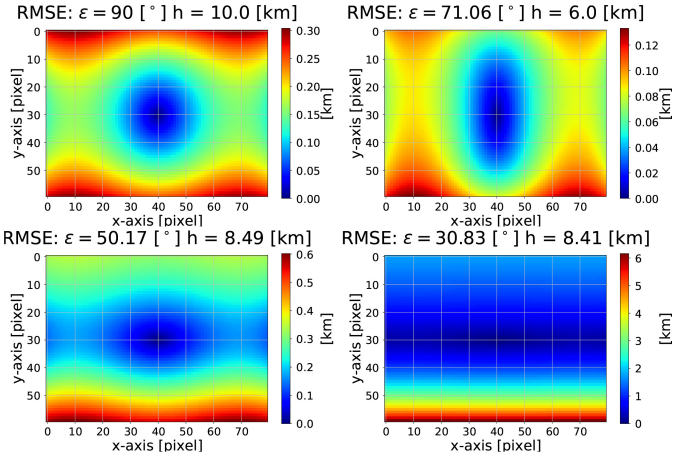

Fig. 7. RMSE between the atmosphere cross section coordinates approximated using the *flat* Earth assumption reprojection and the *great* circle approach reprojection. The coordinates of each reprojection are displayed in Figs. 4 and 5 respectively.

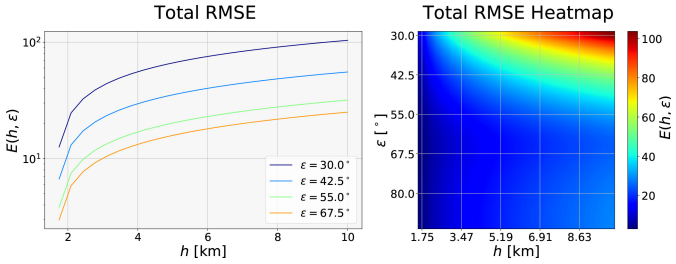

Fig. 8. (Left) Increase in the quadratic total sum of error as a function of the height for four different elevation angles: 30°, 42.5°, 55°, and 67.5°. The error function is in (24). (Right) Quadratic total sum of errors as a function of the elevation angle and the height.

various elevations as a function of h, and Fig. 8 (right) shows a heatmap of the total RMSE as a function of h and ε. As the elevation angle decreases, the region of the atmosphere that is measured in each pixel increases (i.e., perspective). Consequently, the great circle approach performs a more accurate approximation of the cross section plane of the atmosphere in which the clouds are moving.

The atmosphere cross section projected on the Earth's surface using the *great* circle approach reprojection is shown in Fig. 9 in geographic coordinates system (GCS). The GCS components are longitude and latitude on a sphere with the radius $r + h$ (where r is the Earth radius and h is the cloud height), they are defined in degrees. The atmosphere cross section plane is considerably larger when the Sun's elevation angle is low. The distance between pixels in an image increases exponentially from top to bottom.

The results presented in this investigation show that the proposed methodology is advantageous with respect to other methods available in the literature from a theoretical and technological point of view. The geometric reprojection proposed in [28] (i.e., voxel carving) is equivalent to the *flat* Earth approximation investigated in this research, and thus it does not consider the curvature of the Earth (i.e., *great* circle approach). As is demonstrated in this research

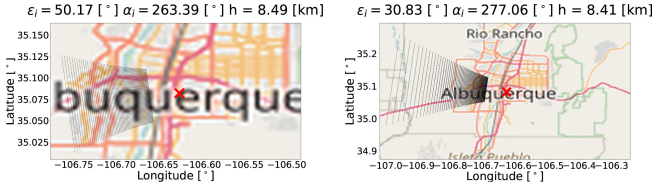

Fig. 9. Atmosphere cross section plane projected on the Earth's surface for elevations of 50.17° and 30.83° using the *great* circle approach (see Fig. 6). The sky imager location is the red dot. The sky imager pixels are in black. The coordinates of a pixel are defined by a longitude and latitude angle.

(see Fig. 7), the order of magnitude of the error produced by this approximation is in the range of kilometers for high clouds (e.g., stratus) measured by pixels with elevation angles <30°. In addition, low-cost radiometric far IR cameras provide temperature measurements (see [29]) which can be transformed to height measurements [30] when combined with weather features measured by a simple weather station in the ground [31]. Radiometric IR cameras have low resolution [24], but their resolution is sufficient to perform accurate intrahour solar forecasting [32].

IV. Conclusion

Intrahour solar forecasting algorithms utilize consecutive sky images to compute cloud velocity vectors, anticipating when a cloud will occlude the Sun and produce a decrease in the GSI that reaches the Earth's surface. Velocity vectors are calculated in units of pixels per frame, but the dimensions of the pixels in sky images vary with the elevation angle. Therefore, the velocity vector accuracy used to forecast cloud occlusions of the Sun can be improved. The proposed perspective reprojection of the imager plane to the geospatial atmosphere cross section plane can be used to transform the pixels in sky images to the cross section coordinate system of the clouds.

When used in sky imagers, thermal images are advantageous in that cloud height can be approximated when cloud temperature is known. Radiometric IR cameras composed of microbolometers are an inexpensive technology capable of acquiring thermal sky images. When intersected by the sky imaging system FOV, the dimensions of the atmosphere cross section plane can be determined using the proposed reprojections and temperatures of the objects in the images.

V. Data Availability

The procedure to acquire and preprocessing the radiometric far IR sky images, plus the hardware was described in [24]. The data used in this work is publicly available in a DRYAD repository (https://doi.org/10.5061/dryad.zcrjdfn9m). The software for both geospatial perspective reprojections is available in a GitHub repository (https://github.com/gterren/geospatial_perspective_reprojection).

Acknowledgment

Authors would like to thank the UNM Center for Advanced Research Computing (CARC), supported in part by NSF, for

providing the high performance computing and large-scale storage resources used in this work. We would also like to thank Marie R. Fernandez for proofreading the manuscript.

REFERENCES

[1] P. Tzoumanikas, E. Nikitidou, A. F. Bais, and A. Kazantzidis, "The effect of clouds on surface solar irradiance, based on data from an all-sky imaging system," *Renew. Energy*, vol. 95, pp. 314–322, Sep. 2016.

[2] H. Wen, Y. Du, X. Chen, E. Lim, H. Wen, L. Jiang, and W. Xiang, "Deep learning based multistep solar forecasting for PV ramp-rate control using sky images," *IEEE Trans. Ind. Informat.*, vol. 17, no. 2, pp. 1397–1406, Feb. 2021.

[3] A. Mammoli, A. Ellis, A. Menicucci, S. Willard, T. Caudell, and J. Simmins, "Low-cost solar micro-forecasts for PV smoothing," in *Proc. 1st IEEE Conf. Technol. Sustain. (SusTech)*, Aug. 2013, pp. 238–243.

[4] Y. Chu, M. Li, and C. F. M. Coimbra, "Sun-tracking imaging system for intra-hour DNI forecasts," *Renew. Energy*, vol. 96, pp. 792–799, Oct. 2016.

[5] G. Terrén-Serrano and M. Martínez-Ramón, "Comparative analysis of methods for cloud segmentation in ground-based infrared images," *Renew. Energy*, vol. 175, pp. 1025–1040, Sep. 2021.

[6] C. W. Chow *et al.*, "Intra-hour forecasting with a total sky imager at the UC San Diego solar energy testbed," *Solar Energy*, vol. 85, no. 11, pp. 2881–2893, 2011.

[7] B. J. Redman, J. A. Shaw, P. W. Nugent, R. T. Clark, and S. Piazzolla, "Reflective all-sky thermal infrared cloud imager," *Opt. Exp.*, vol. 26, no. 9, pp. 11276–11283, Apr. 2018.

[8] M. I. Gohari *et al.*, "Comparison of solar power output forecasting performance of the total sky imager and the University of California, San Diego sky imager," *Energy Proc.*, vol. 49, pp. 2340–2350, Jan. 2014.

[9] R. Marquez and C. F. M. Coimbra, "Intra-hour DNI forecasting based on cloud tracking image analysis," *Sol. Energy*, vol. 91, pp. 327–336, May 2013.

[10] Q. Li, W. Lu, J. Yang, and J. Z. Wang, "Thin cloud detection of all-sky images using Markov random fields," *IEEE Geosci. Remote Sens. Lett.*, vol. 9, no. 3, pp. 417–421, May 2012.

[11] S. Liu, L. Zhang, Z. Zhang, C. Wang, and B. Xiao, "Automatic cloud detection for all-sky images using superpixel segmentation," *IEEE Geosci. Remote Sens. Lett.*, vol. 12, no. 2, pp. 354–358, Feb. 2015.

[12] H.-Y. Cheng and C.-L. Lin, "Cloud detection in all-sky images via multi-scale neighborhood features and multiple supervised learning techniques," *Atmos. Meas. Techn.*, vol. 10, no. 1, pp. 199–208, 2017.

[13] L. Ye, Z. Cao, Y. Xiao, and Z. Yang, "Supervised fine-grained cloud detection and recognition in whole-sky images," *IEEE Trans. Geosci. Remote Sens.*, vol. 57, no. 10, pp. 7972–7985, Oct. 2019.

[14] C. Shi, Y. Zhou, B. Qiu, J. He, M. Ding, and S. Wei, "Diurnal and nocturnal cloud segmentation of all-sky imager (ASI) images using enhancement fully convolutional networks," *Atmos. Meas. Techn.*, vol. 12, no. 9, pp. 4713–4724, Sep. 2019.

[15] M. Caldas and R. Alonso-Suárez, "Very short-term solar irradiance forecast using all-sky imaging and real-time irradiance measurements," *Renew. Energy*, vol. 143, pp. 1643–1658, Dec. 2019.

[16] M. Hasenbalg, P. Kuhn, S. Wilbert, B. Nouri, and A. Kazantzidis, "Benchmarking of six cloud segmentation algorithms for ground-based all-sky imagers," *Sol. Energy*, vol. 201, pp. 596–614, May 2020.

[17] A. Mammoli, G. Terrén-Serrano, A. Menicucci, T. P. Caudell, and M. Martínez-Ramón, "An experimental method to merge far-field images from multiple longwave infrared sensors for short-term solar forecasting," *Sol. Energy*, vol. 187, pp. 254–260, Jul. 2019.

[18] J. Nummikoski, "Sky-image based intra-hour solar forecasting using independent cloud-motion detection and ray-tracing techniques for cloud shadow and irradiance estimation," M.S. thesis, Dept. Electron. Commun. Eng., Univ. Texas, San Antonio, TX, USA, 2013.

[19] W. Richardson, H. Krishnaswami, R. Vega, and M. Cervantes, "A low cost, edge computing, all-sky imager for cloud tracking and intra-hour irradiance forecasting," *Sustainability*, vol. 9, no. 4, p. 482, Mar. 2017.

[20] D. A. Nguyen and J. Kleissl, "Stereographic methods for cloud base height determination using two sky imagers," *Sol. Energy*, vol. 107, pp. 495–509, Sep. 2014.

[21] P. Kuhn *et al.*, "Benchmarking three low-cost, low-maintenance cloud height measurement systems and ECMWF cloud heights against a ceilometer," *Sol. Energy*, vol. 168, pp. 140–152, Jul. 2018.

[22] G. Wang, B. Kurtz, and J. Kleissl, "Cloud base height from sky imager and cloud speed sensor," *Sol. Energy*, vol. 131, pp. 208–221, Jun. 2016.

[23] G. C. Wang, B. Urquhart, and J. Kleissl, "Cloud base height estimates from sky imagery and a network of pyranometers," *Sol. Energy*, vol. 184, pp. 594–609, May 2019.

[24] G. Terrén-Serrano, A. Bashir, T. Estrada, and M. Martínez-Ramón, "Girasol, a sky imaging and global solar irradiance dataset," *Data Brief*, vol. 35, Apr. 2021, Art. no. 106914.

[25] G. Terrén-Serrano and M. Martínez-Ramón, "Multi-layer wind velocity field visualization in infrared images of clouds for solar irradiance forecasting," *Appl. Energy*, vol. 288, Apr. 2021, Art. no. 116656.

[26] M. H. Ambaum, *Thermal Physics of the Atmosphere*. Amsterdam, The Netherlands: Elsevier, 2020.

[27] T. L. Heath *et al.*, *The Thirteen Books of Euclid's Elements*. Chelmsford, MA, USA: Courier Corporation, 1956.

[28] B. Nouri *et al.*, "Cloud height and tracking accuracy of three all sky imager systems for individual clouds," *Sol. Energy*, vol. 177, pp. 213–228, Jan. 2019.

[29] P. M. Lewis, H. Rogers, and R. H. Schindler, "A radiometric all-sky infrared camera (RASICAM) for DES/CTIO," *Proc. SPIE*, vol. 7735, Jul. 2010, Art. no. 77353C.

[30] P. H. Stone and J. H. Carlson, "Atmospheric lapse rate regimes and their parameterization," *J. Atmos. Sci.*, vol. 36, no. 3, pp. 415–423, Mar. 1979.

[31] G. Terrén-Serrano and M. Martínez-Ramón, "Processing of global solar irradiance and ground-based infrared sky images for solar nowcasting and intra-hour forecasting applications," 2021, *arXiv:2101.08694*.

[32] G. Terrén-Serrano and M. Martínez-Ramón, "Review of kernel learning for intra-hour solar forecasting with infrared sky images and cloud dynamics feature extraction," 2021, *arXiv:2110.05622*.

Guillermo Terrén-Serrano received the bachelor's degree in technical industrial engineering with emphasis in electricity from the Universidad de Zaragoza, Zaragoza, Spain, in 2012, and the M.S. degree in power and energy from The University of New Mexico, Albuquerque, NM, USA, in 2016, where he is currently pursuing the Ph.D. degree with the Department of Electrical and Computer Engineering.

His research interests include computer vision, image processing, machine learning, smart grids, solar forecasting, and sky imagers.

Manel Martínez-Ramón (Senior Member, IEEE) received the degree in telecommunications engineering from the Universitat Politècnica de Catalunya, Barcelona, Spain, in 1996, and the Ph.D. degree in communications technologies from the Universidad Carlos III de Madrid, Madrid, Spain, in 1999.

He is currently a Professor with the Department of Electrical and Computer Engineering, The University of New Mexico, Albuquerque, NM, USA. He holds the King Felipe VI Endowed Chair of The University of New Mexico, a chair sponsored by the Household of the King of Spain. His research interests include machine learning applications to smart antennas, neuroimage, and smart grids.